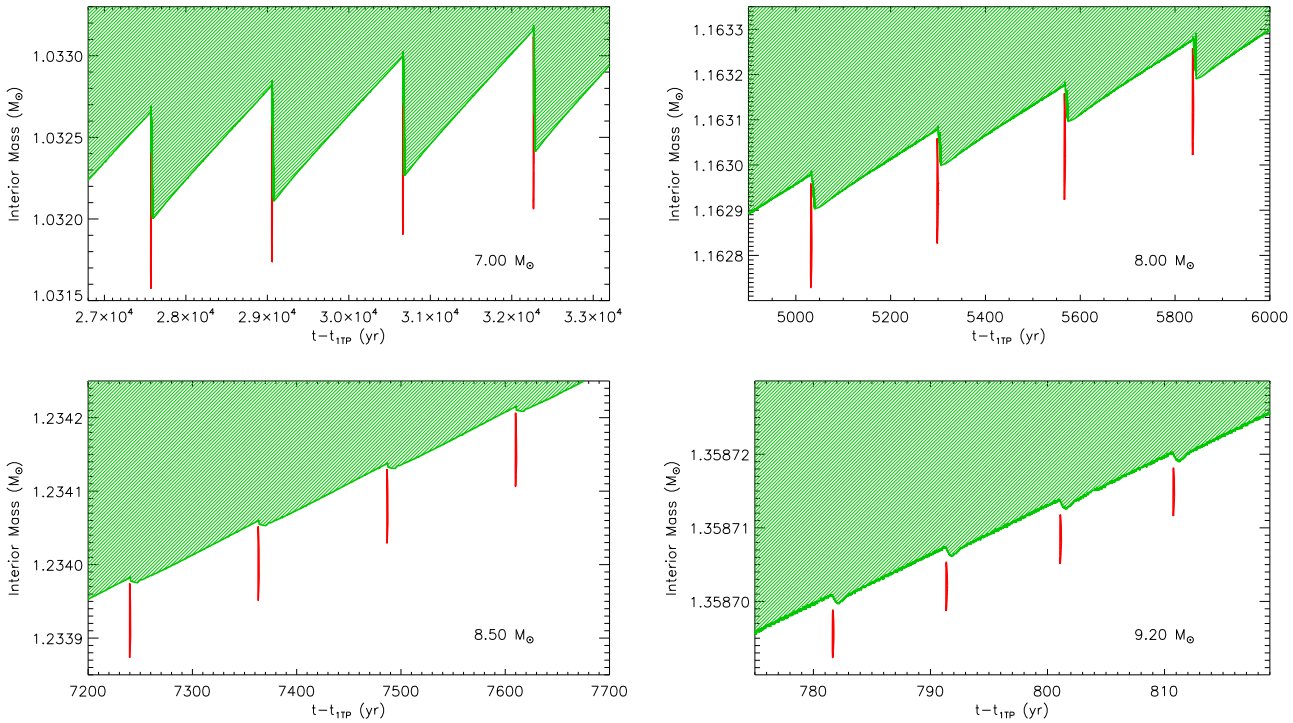

Figure 11. Evolution of the convective envelope (green shaded area) and the He convective shell (red line) as a function of time during the last four thermal pulses for the AGB 7.0 $M_{\odot}$ model (upper left panel) and the 8.0, 8.5, and 9.2 $M_{\odot}$ SAGB models, (upper right, lower left, and lower right panels, respectively). The time has been reset at the core He exhaustion.

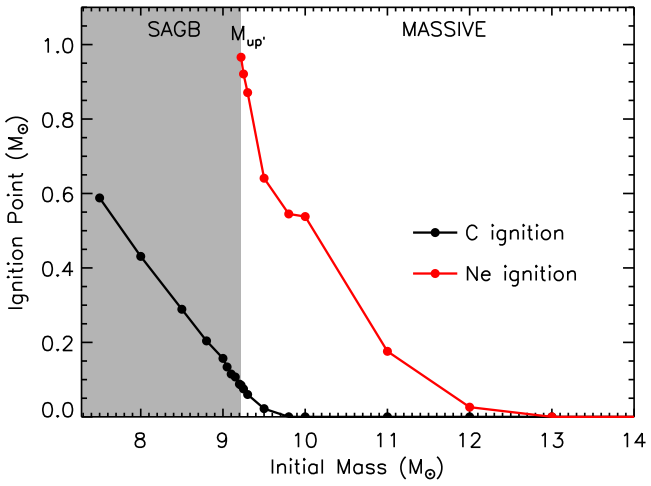

Figure 12. Ignition mass coordinate of C (black line and dots) and Ne burning (red line and dots) as a function of the initial mass (see legend).

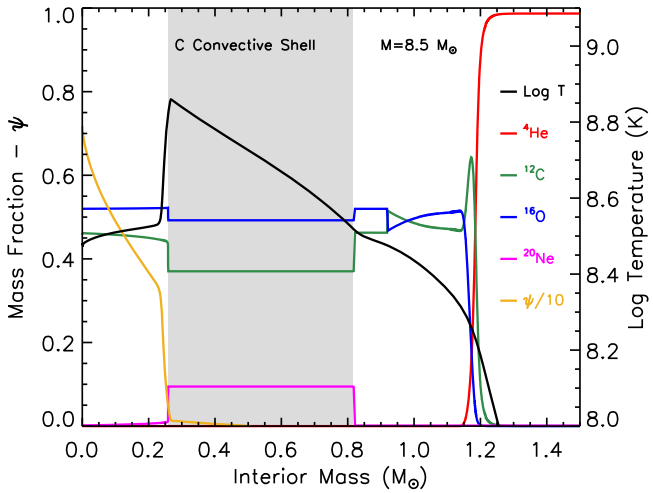

Figure 13. Selected interior properties of a 8.5 $M_{\odot}$ model during the off-center C burning (see the legend). The chemical composition and degeneracy parameter are reported on the left y-axis, while the temperature is reported on the right y-axis. The degeneracy parameter is divided by 10 in order to improve the readability.

amount of matter per second. This stage ends with the onset of the thermal pulses (see next section and also Sugimoto & Nomoto 1975, for discussion on the evolution of this phase).

In stars with initial mass $9.22 \leqslant M/M_{\odot} \leqslant 10.00$, neon burning is ignited off-center during the second dredge-up and before the bottom of the convective envelope enters into the region enriched by the He-burning products (see also Nomoto 1984). Once neon is ignited, the evolution of the star becomes fast enough that the zones above the He cores remain essentially frozen. For this reason, in these stars, the products of He burning are never brought to the surface; therefore, no increase of the surface ^{12}C is found.

3.6. Evolution during the TP-SAGB Phase: Stars with Mass $7.5 \leqslant M/M_{\odot} \leqslant 9.20$

After the H-burning shell has been reignited, stars in the mass range $7.5 \leqslant M/M_{\odot} \leqslant 9.20$ enter a classical TP phase, where the two H and He shells alternatively activate above a degenerate ONeMg core that is surrounded by a thin zone enriched in CO, the latter left by the He-burning shell. The general properties of these stars during this phase, named TP-SAGB, have been reviewed and described in detail in the literature (see Section 1); therefore, we will focus here mainly on how these properties change as a function of the initial mass.

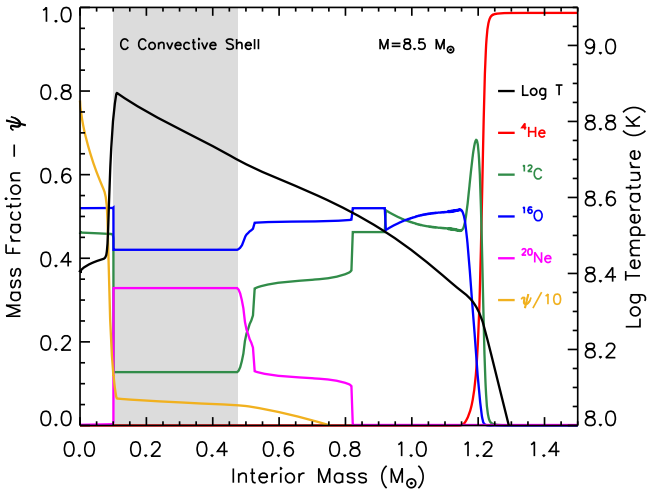

Figure 14. Selected interior properties of a 8.5 $M_{\odot}$ model during the off-center C burning (see the legend). The chemical composition and degeneracy parameter are reported on the left y-axis, while the temperature is reported on the right y-axis. The degeneracy parameter is divided by 10 in order to improve the readability.

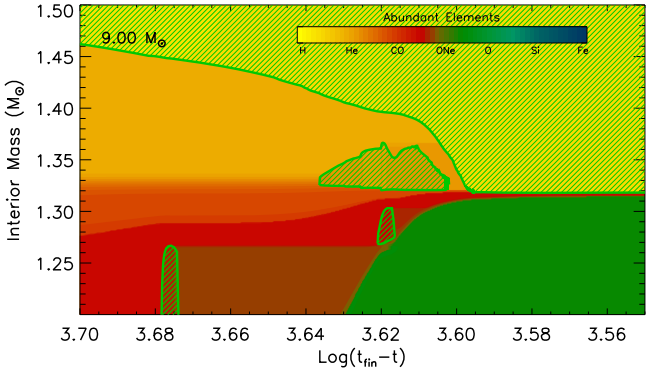

Figure 15. Convective (green shaded areas) and chemical (color codes reported in the color bar) internal history of the 9 $M_{\odot}$ model during the late phase of the second dredge-up. The x-axis reports the logarithm of the time until the end of the evolution ($t_{\rm fin} - t$) in units of years.

The main evolutionary properties during the TP-SAGB phase of stars in this mass interval ($7.5 \leqslant M/M_{\odot} \leqslant 9.20$) are reported in Table 4.

In general, each thermal pulse is characterized by the following phenomena: (1) a strong activation of the He-burning reactions followed by the formation of a He convective zone and a peak in the He luminosity ($L_{\rm He}$); (2) the disappearance of the He convective zone and the steady He-shell burning phase that accretes the CO core; (3) the switching off of the H-burning shell; (4) the penetration of the convective envelope that may in some cases erode the He core (third dredge-up); (5) the reactivation of the H shell and the switching off of the He-burning shell; and (6) the steady H-shell burning phase, where the He core increases and the convective envelope recedes in mass (interpulse phase) until the next pulse is ignited. A schematic view of this phase can be found, e.g., in Doherty et al. (2017; Figure 5).

Figure 7 shows the luminosity of the H- and He-burning shells as a function of time for the AGB and selected SAGB models. Moving from AGB stars ($M = 7.0\,M_{\odot}$) to SAGB stars ($7.5 \leqslant M/M_{\odot} \leqslant 9.20$), the maximum luminosity of the He-burning shell reached during each thermal pulse decreases, while the frequency of the TPs increases. This is due to the fact that the core mass becomes more massive and hotter as the initial mass of the star increases (see Doherty et al. 2017 and references therein). The increase of both the ^{4}He and ^{12}C abundance after the second dredge-up contributes to increasing the frequency of the thermal pulses in stars with initial mass $M \geqslant 8.5\,M_{\odot}$ because it makes the H shell more efficient.

Figure 11 shows a zoom of selected models during the last few computed thermal pulses. Moving from the 7 to the 9.2 $M_{\odot}$ model, the following are worth noting: (1) the reduction of the size of the He convective shell from $\sim 10^{-4}$ to $\sim 10^{-5}\,M_{\odot}$, (2) the strong reduction of the interpulse time from $\sim 10^{3}$ to ~ 10 yr, and (3) the progressive reduction of the third dredge-up that disappears in stars with mass $M \geqslant 9.0\,M_{\odot}$. It is also worth mentioning that, in general, the higher the mass, the higher the number of thermal pulses occurring before the beginning of the formation of a He convective shell associated with each thermal pulse (see Table 4).

Figure 9 shows that the maximum temperature reached at the base of the convective envelope ($T_{\rm BCE}$) is in the range 80–110 MK and scales roughly with the initial mass; i.e., the larger the mass, the larger the $T_{\rm BCE}$. In general, this quantity increases slightly during the TP phase, but it may also show a nonmonotonic behavior as a function of time if some other energy sources are activated inside the CO core, as in the case of the more massive models ($M \geqslant 9.05\,M_{\odot}$), where the URCA processes become efficient (see below).

The mass loss during this phase plays a key role because it competes with the increase of the CO core in reducing the H-rich envelope and therefore in determining the duration of the TP phase. The typical mass-loss rate averaged over the last few thermal pulses is in the range 1–3 $\sim 10^{-5}\,M_{\odot}\,{\rm yr}^{-1}$, the higher values reached by the more massive models.

The computations are stopped after a sufficient number of thermal pulses have been computed to safely extrapolate the evolution of these stars during the TP phase (see Section 3.8).

3.7. Stars with Mass $9.05 \leqslant M/M_{\odot} \leqslant 9.20$: URCA Processes

In stars with more massive ONeMg degenerate cores ($9.05 \leqslant M/M_{\odot} \leqslant 9.20$), the density increases enough (Figure 16) that the Fermi energy becomes close to the threshold value for the ECs on a number of nuclear species that are quickly followed by beta decays. In this situation, given two generic nuclear species, $N(A,\ Z)$ and $M(A,\ Z-1)$, the two reactions $N(A,\ Z) + e^{-} \rightarrow M(A, Z-1) + \nu$ and $M\,(A,\ Z\ -\ 1) \rightarrow N\,(A,\ Z)\ +\ e^{-}\ +\ \bar{\nu}$, written in a compact form as $^{A}(N,\ M)$, are in equilibrium. The reaction pair $^{A}(N,\ M)$ is called the URCA process.

The effect of the activation of an URCA process can be explained with the aid of Figure 17, which shows the properties of a model in which a generic URCA pair $^{A}(N,\ M)$ is efficient. If we define λ as the number of captures/decays per unit time, the lower left panel shows that as the density decreases (i.e., the interior mass increases), the EC rate ($\lambda_{\rm ec}$; black solid line) decreases, while the beta decay rate (λ_{β}; black dashed line) increases. The density at which $\lambda_{\rm ec} = \lambda_{\beta}$ is called the URCA shell ($\rho_{\rm crit}$) and is marked in all of the panels of Figure 17 by a vertical dashed line. Inside the mass coordinate corresponding to the URCA shell, $\rho > \rho_{\rm crit}$ and $\lambda_{\rm ec} \gg \lambda_{\beta}$. Outside the URCA shell, on the contrary, $\rho < \rho_{\rm crit}$ and $\lambda_{\rm ec} \ll \lambda_{\beta}$. As mentioned above, in this situation, the two reactions are in equilibrium, which means that the number of reactions occurring per unit mass and unit time r of the two processes coincide ($r_{\rm ec} = r_{\beta}$) and show a maximum corresponding to the URCA shell. Since

$r = \lambda Y$ (where $Y = X/A$ is the abundance by number, X is the abundance in mass fraction, and A is the atomic weight), this also implies that the equilibrium abundances of the two nuclei satisfy the relation $Y(N)/Y(M) = \lambda_\beta/\lambda_{ec}$. As a consequence, $X(M) \gg X(N)$ inside the URCA shell, while $X(N) \gg X(M)$ outside the URCA shell (upper left panel in Figure 17).

The energy released by the EC, E_{ec}, and the beta decay, E_β, are given by (see Miyaji et al. 1980; Suzuki et al. 2016)

$$E_{ec} = Q_{nuc} - E_\nu + \mu_e$$
$$E_\beta = Q_{nuc} - E_\nu - \mu_e,$$

where Q_{nuc} is the mass defect between reactants and products, E_ν is the neutrino energy loss (in absolute value), and μ_e is the chemical potential of the electrons. When an URCA pair is in equilibrium $r_{ec} = r_\beta$, therefore, the total net energy released per unit mass and unit time in this case will be simply $\varepsilon = -r[E_{\nu,ec} + E_{\nu,\beta}]$; i.e., it will be always negative and will show a deep minimum corresponding roughly to the URCA shell (lower right panel of Figure 17). Thus, in general, we can identify inside a model various cooling zones associated with the URCA shells of the various URCA pairs. It goes without saying, however, that only URCA pairs involving nuclear species with sizable abundances will have some effect on the evolution of the model. In addition to that, as the core of the star contracts, the density increases, and the URCA shell of any given URCA pair shifts outward in mass and constitutes an outward-moving "cooling wave."

Having said this, in the following, we will first describe the evolution of the 9.2 $M_\odot$ model. As the central density increases above $\log[\rho_c\ (\mathrm{g\ cm^{-3}})] \sim 9.0$, two URCA pairs activate and produce some effect on the interior of the star. The first one is ^{25}(Mg, Na), at density $\log[\rho_c\ (\mathrm{g\ cm^{-3}})] \sim 9.11$, while the second one is ^{23}(Na, Ne), at density $\log[\rho_c\ (\mathrm{g\ cm^{-3}})] \sim 9.25$. The effect of each URCA pair episode at the center is that of a cooling phase, followed by a roughly isothermal evolution (black line in Figure 16). The cooling phase corresponds to the stage when the central density is close to the URCA shell ($\rho_c \sim \rho_{crit}$), while the isothermal evolution corresponds to the stage when the URCA shell leaves the center and shifts outward in mass. In order to describe these phases in more detail, we show in Figure 18 some properties of the center of the model during the activation of the ^{25}(Mg, Na) pair, i.e., the first important URCA pair.

As the central density approaches the URCA shell, the nuclear energy (ε_n) that, as already mentioned above, is dominated by the neutrino emission due to the URCA pair ($-E_\nu$) decreases dramatically. During this phase, the gravitational energy (ε_g) increases, while the (thermo)neutrino losses (ε_ν) progressively decrease due to the lowering of the central temperature, and the net result is that the total energy is negative. This implies a substantial reduction of the central temperature (T_c). As the central density continues to increase ($\rho_c > \rho_{crit}$), the URCA shell leaves the center and moves outward in mass (driving an outward-moving cooling wave); therefore, in the center, the nuclear energy begins to increase toward the values it had before the activation of the URCA pair (i.e., it tends toward ~0). During this phase, the gravitational energy decreases progressively, partially reabsorbing the increase of the nuclear energy, while the neutrino energy losses become negligible compared to the nuclear and gravitational energies because of the low temperature. The

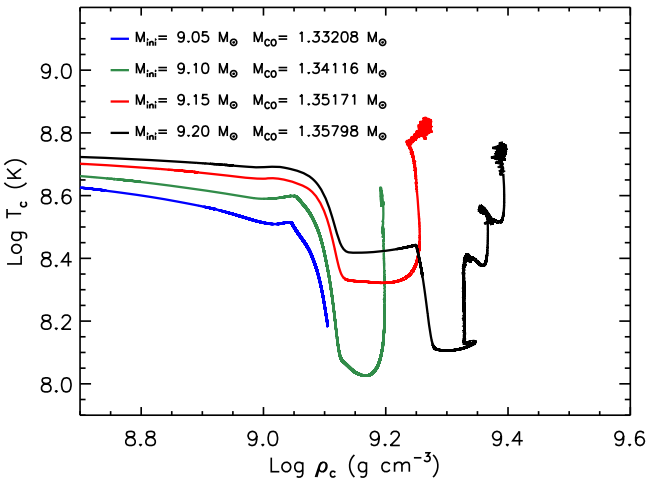

Figure 16. Central temperature as a function of the central density during the late stages of models in which the URCA processes are activated.

net effect is that in this phase, the total energy progressively increases toward less negative values. The energy imbalance between the center and the location of the URCA shell also produces an increase in the radiative gradient in the core (see dashed, dotted, and long-dashed lines in Figure 19). When the central density becomes higher than $\log[\rho_c\ (\mathrm{g\ cm^{-3}})] \sim 9.141$, the total net energy becomes positive, the radiative gradient overcomes the adiabatic one, and the center of the star becomes convective. Note that the gradient of chemical composition around the center is not high enough to stabilize the zone against the onset of convection (Figure 19). This is also confirmed by a test evolution in which we adopted the Ledoux criterion during this phase. Jones et al. (2013), Takahashi et al. (2013), and Zha et al. (2019) did not find the formation of the convective core in their models. Such a difference might be due to the difference in the treatment of convection and the zoning, which could affect the gradient of the chemical composition, in the evolutionary codes.

When the convective core sets in, it has a strong effect on the equilibrium of the URCA pair reaction. The reason is the following. In a radiative environment, the ^{25}Mg abundance in the central zones is the result of the equilibrium between EC and beta decay and has an increasing profile from the center toward the URCA shell (like the one shown in the upper left panel of Figure 17). Once convection sets in, it forces the ^{25}Mg abundance to increase in the inner zones and decrease in the outer ones compared to the radiative case (compare the upper left panels of Figures 17 and 20). As a consequence, the two reactions of the ^{25}(Mg, Na) pair are no longer in equilibrium, but, on the contrary, $r_{ec} > r_\beta$ in roughly the inner half of the convective core, while $r_{ec} < r_\beta$ in the outer half (solid and dashed green lines in the figure). In this case, the total net energy released per unit mass and unit time is given by $r_{ec}E_{ec} + r_\beta E_\beta$. Since E_{ec} is positive in roughly the inner half of the convective core and negative outward in mass, while E_β is always negative (see the solid and dashed red lines in the lower left panel of Figure 20), the total energy released by the ^{25}(Mg, Na) pair is positive in roughly the inner half of the convective core and negative in the remaining half (see the orange line in the lower right panel in the figure), with the zero value roughly corresponding to the mass coordinate where $r_{ec} = r_\beta$. The continuous ingestion of a higher ^{25}Mg abundance from the outer radiative layers produces an increase of the nuclear

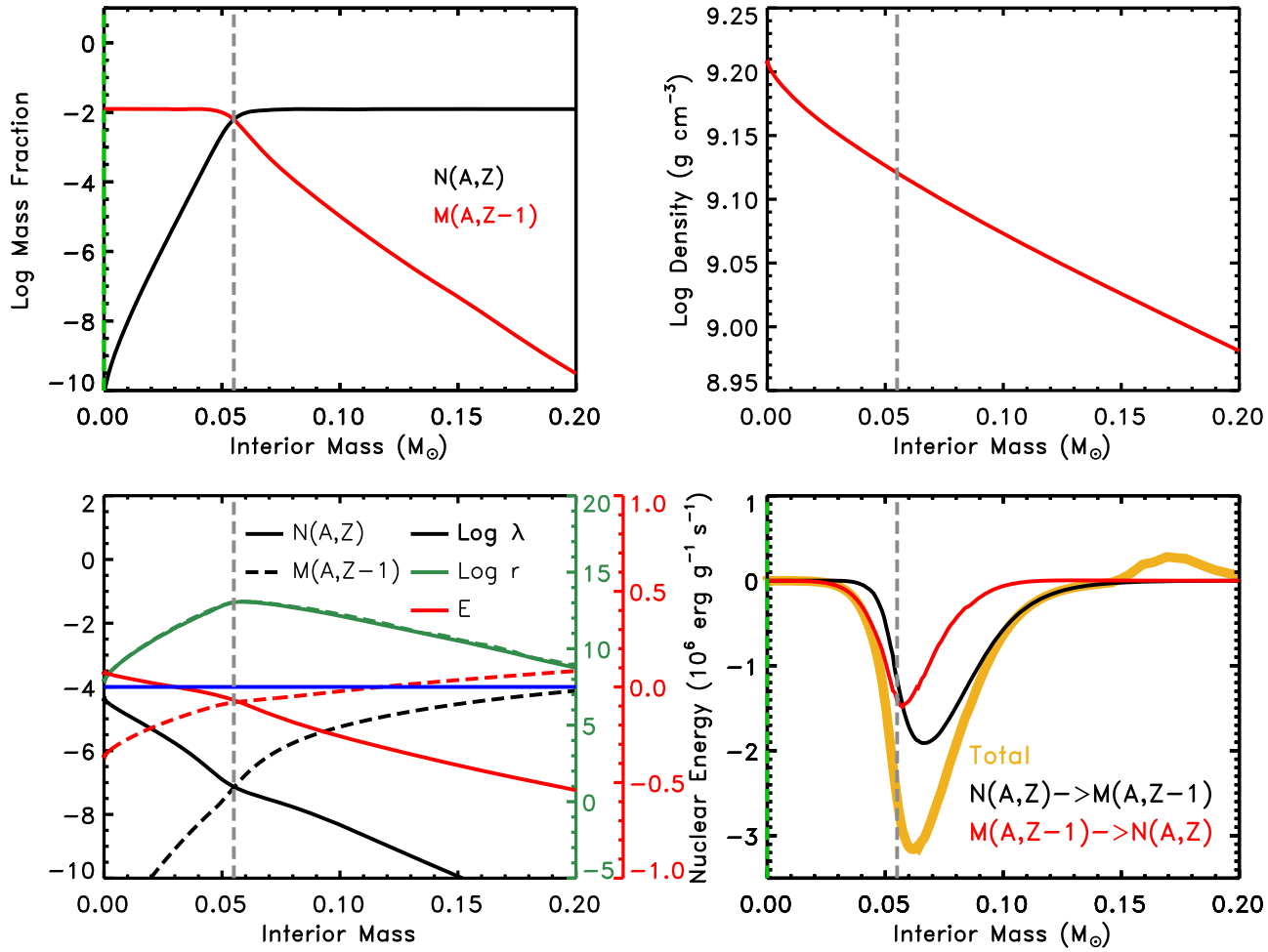

Figure 17. Selected properties of a model in which a generic URCA pair $^{A}(N, M)$ is efficient. Upper left panel: abundance in mass fraction as a function of the interior mass of the two interacting nuclei N and M. Upper right panel: density as a function of the interior mass. Lower left panel: number of captures/decays per unit time in seconds (λ; black lines, right y-axis), number of reactions occurring per unit mass and unit time in grams per second (r; green lines, right y-axis), and nuclear energy of the URCA pair in MeV (E; red lines, right y-axis); the solid lines refer to the EC, while the dashed lines refer to the beta decay. Lower right panel: nuclear energy of the URCA pair in ergs per unit mass and unit time ($\varepsilon = -rE_{\nu}$); the black line refers to the EC, the red line to the beta decay, and the orange line to the total of the URCA pair. In all of the panels, the gray vertical dashed line marks the URCA shell.

energy close to the center that induces the convective zone to extend even more, driving in this way a progressive increase of the convective core (Figure 19). During the phase characterized by the increase of the convective core, the central density increases progressively at almost constant temperature (Figure 20).

When the central density approaches $\log[\rho_c\ (\mathrm{g\ cm^{-3}})] \sim 9.248$, the URCA pair ^{23}(Na, Ne) starts activating and producing some effects on the structure of the star. The evolution of the center during this phase is similar to that already discussed for the ^{25}(Mg, Na) pair. The initial phase is characterized by a cooling, due to the EC on ^{23}Na, that makes the center of the star radiative and forces the convective core driven by the ^{25}(Mg, Na) pair to become a convective shell that shifts progressively outward in mass. Then, after the URCA shell of the pair ^{23}(Na, Ne) leaves the center and moves outward in mass, a convective core forms that increases progressively in mass while the center contracts at almost constant temperature (Figure 16). A typical model during this phase is shown in Figures 21 and 22. The inner $0.02\,M_{\odot}$ zones are convective and show the typical behavior already discussed in the case of the ^{25}(Mg, Na) pair. In particular, the rate of the EC on ^{23}Na dominates over the decay of the ^{23}Ne in approximately the inner half of the convective core, while the ^{23}Ne decay prevails on the EC on ^{23}Na in the remaining half. As a consequence, the nuclear energy is positive in the zones where the EC dominates and negative where the beta decay prevails. Inside the convective core, ^{23}Ne is much more abundant than ^{23}Na, which, on the contrary, dominates in the outer radiative layers. During this phase, the convective shell driven by the ^{25}(Mg, Na) URCA pair is roughly confined between the ^{23}(Na, Ne) URCA shell at the bottom and the ^{25}(Mg, Na) URCA shell at the top. Also note the radiative zone that separates the convective core and the convective shell; in this zone, $r_{\rm ec} = r_{\beta}$. It is worth mentioning at this point that a similar evolution has already been found by Ritossa et al. (1999). In particular, in their Figure 25, they show the properties of their last computed model characterized by a convective core driven by the ^{23}(Na, Ne) pair and a convective shell driven by the ^{25}(Mg, Na) pair. The chemical composition and the various contributions to the total energy generation are extremely similar to what we find. In particular, they also find that in each convective region, the URCA pair releases positive energy in the inner zone and negative energy in the outer layers (see panel (c) in their Figure 25). At variance with what we and Ritossa et al. (1999) find, the formation of a convective core

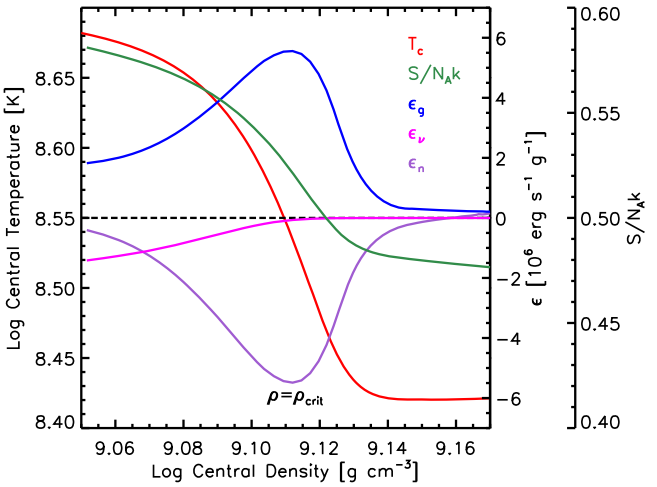

Figure 18. Selected central quantities as a function of the central density of the 9.2 $M_\odot$ model during the activation of the ^{25}(Mg, Na) pair: temperature (red line, left y-axis), adimensional entropy per baryon (green line, right y-axis), and nuclear (purple), gravitational (blue), and neutrino (magenta) energies (right y-axis).

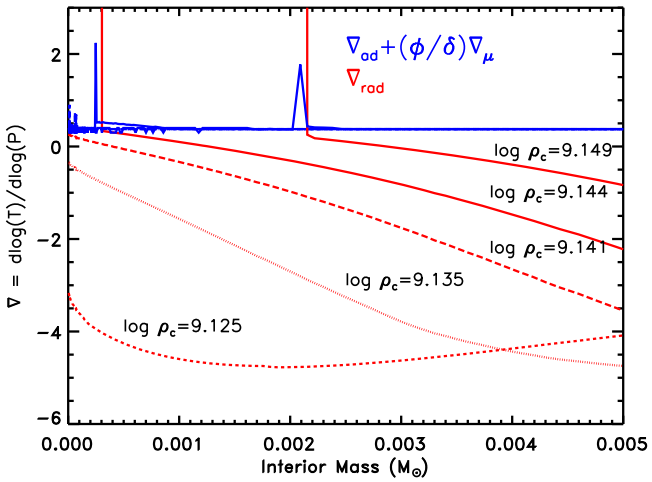

Figure 19. Temperature gradients (see the legend) as a function of the interior mass of the 9.2 $M_\odot$ star at selected times during the formation of the convective core associated with the ^{25}(Mg, Na) URCA pair, marked by the values of the central densities in units of g cm^{-3}. According to the adopted stability criterion (see text), convection sets in when the radiative gradient becomes larger than the adiabatic one. Let us remember that the actual temperature gradient used is the adiabatic one in the convective zones and the radiative one in the radiative layers.

and shell during this phase is not addressed by Jones et al. (2013), Takahashi et al. (2013), and Zha et al. (2019). We do not have a clear explanation for that; hence, what we can say is that the origin of such a difference could be due to the difference in the numerical treatment of convection in the stellar evolution code.

The evolution of the center, following the formation of the convective core driven by the ^{23}(Na, Ne) pair, is characterized by an increase of the central temperature at almost constant density interspersed with phases where the density increases at almost constant temperature (black line in Figure 16). The reason for such a behavior is due to the fact that the convective core, after it is formed, begins to progressively increase in mass because of the increase of the nuclear energy produced close to the center due to the ingestion of fresh ^{23}Na present in the outer radiative zones. When the ^{23}Na abundance mixed into the convective core is comparable to or even larger than the one initially present, the increase of the nuclear energy is not reabsorbed; on the contrary, it drives a greater increase of the convective core on a very short timescales, compared to the previous evolution. This is a runaway that looks like the breathing pulse phenomenon occurring during the core He burning (see above). During this phase, the central ^{23}Na mass fraction increases to values as high as $\sim 3 \times 10^{-3}$, i.e., more than 2 orders of magnitude, compared to the abundance present before the beginning of this process (see the first increase of the central ^{23}Na abundance; green line in Figure 23). Since the matter is highly degenerate, the increase of the nuclear energy due to this process induces an increase of the central temperature at constant density (Figure 23). We call this phenomenon "temperature increase due to a runaway" (TIR). The increase of the convective core eventually ceases when the ^{23}Na ingested from the radiative zones is such that it does not significantly alter the nuclear energy. This happens when the mass of the convective core is $\sim$0.06 $M_\odot$. During the following evolution, the excess of the nuclear energy is progressively reabsorbed, and the mass of the convective core and the central temperature remain essentially constant, while the central ^{23}Na abundance progressively decreases toward values similar to those corresponding to the beginning of this process. This stage also coincides with the onset of the thermal pulses. The following evolution of the star is characterized by two other similar processes (see the last two sharp increase of the central temperature in Figure 23) that raise the central temperature to values as high as $\log[T_c\,(\mathrm{K})] \sim 8.8$. During the phase characterized by the thermal pulses, the convective shell driven by the ^{25}(Mg, Na) increases in mass up to $\sim$0.9 $M_\odot$, but this has little effect on the interior of the star (lower right panel in Figure 24).

The calculation of the evolution of this star is then stopped after 102 thermal pulses. The final fate of this star is discussed in the following; however, we anticipate here that, on the basis of the results obtained, it is difficult to envisage whether the center of the star will reach the threshold temperature for the activation of the ^{20}Ne photodisintegration, or the increase of the central temperature will stop and the core will restart contracting until the density thresholds for the activation of the ECs on ^{24}Mg first and on ^{20}Ne later are reached. Moreover, an interaction between the convective core and the convective shell cannot be excluded, with consequences for the evolution of the star that are difficult to predict.

It is interesting to note that the evolution of the center prior to the onset of the TIR discussed above, i.e., until the central density approaches the value $\log[\rho_c\,(\mathrm{g\,cm^{-3}})] \sim 9.35$, is not affected by the efficiency of mixing in the convective zones. Figures 25 and 26, in fact, show that, as long as $\log[\rho_c\,(\mathrm{g\,cm^{-3}})] \leqslant 9.35$, the evolution of both the central density and the central temperature of the standard model (red lines) is almost identical to the one obtained in a test model in which the mixing is artificially suppressed (blue lines). The differences between the two models appear only when the TIR begins in the standard model, i.e., when the red and blue lines begin to differ from each other. The occurrence of this phenomenon has two main effects: it slows down the contraction of the core (Figure 25) and induces an increase of the central temperature (Figure 26) compared to the case in which the chemical mixing is suppressed. For sake of completeness, we also report the results obtained for a test

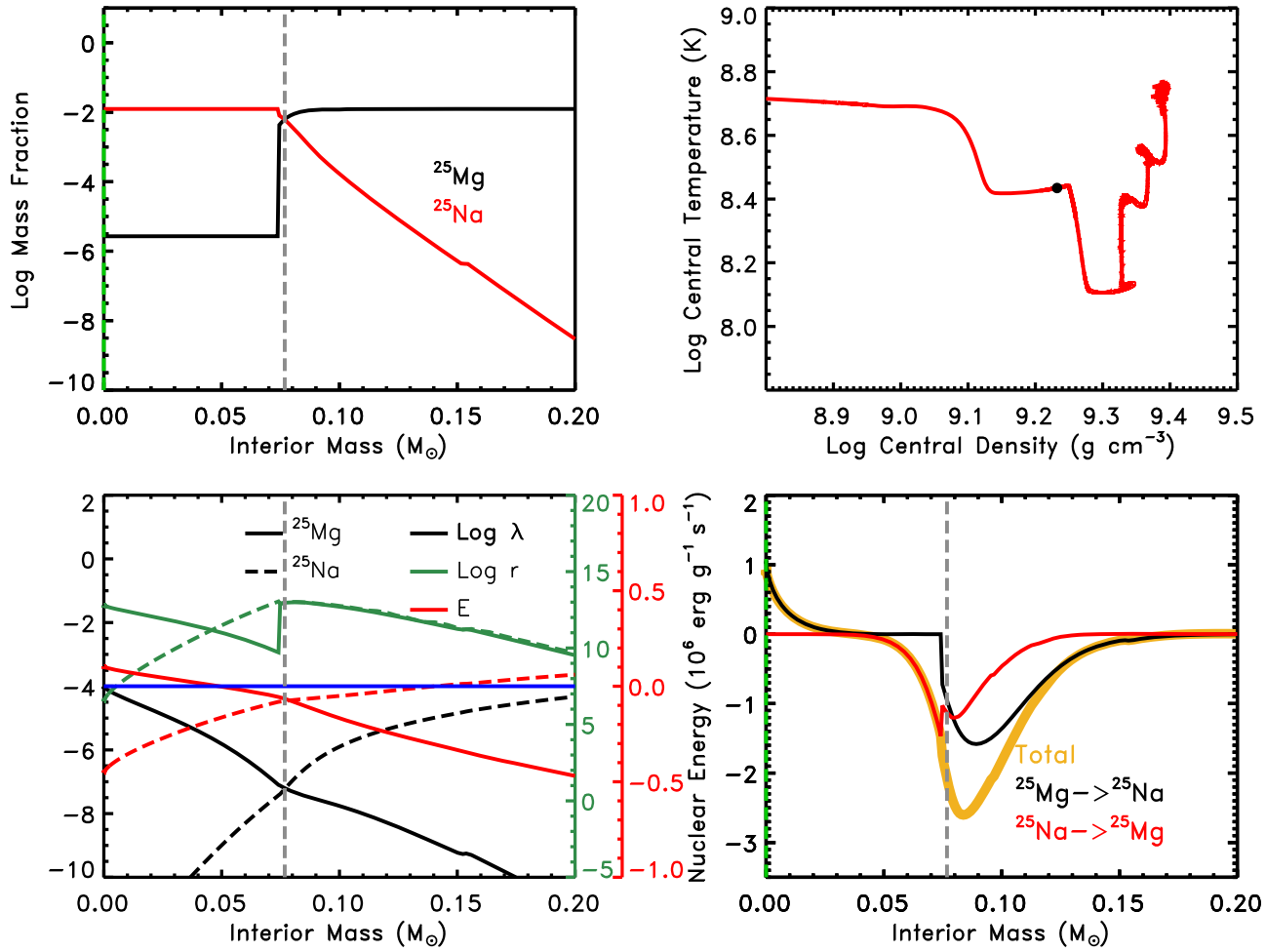

Figure 20. As Figure 17, in the case of a 9.20 $M_{\odot}$ model during the phase in which a convective core induced by the ^{25}(Mg, Na) URCA pair is formed. The vertical gray dashed line marks the ^{25}(Mg, Na) URCA shell.

model in which the URCA processes are not included (green lines in Figures 25 and 26). In this case, the contraction of the core is slower than in the case of the model where the URCA processes are taken into account and mixing is suppressed and similar to the reference case. Moreover, as expected, the activation of the two URCA pairs ^{25}(Mg, Na) and ^{23}(Na, Ne) reduces the central temperature by a factor of ∼3 (at $\log[\rho_c\ (\mathrm{g\ cm^{-3}})] = 9.35$) compared to the model in which the URCA processes are not included. Let us eventually note that, as mentioned above and shown in Figure 26, the TIR is associated with the presence of a convective core and occurs in an advanced phase after its formation. For this reason, this phenomenon is not found either by Ritossa et al. (1999), because they stop the calculation too early, or by Jones et al. (2013), Takahashi et al. (2013), and Zha et al. (2019), because they do not find the formation of the convective core in their models.

The evolution of the center of the 9.15 $M_{\odot}$ model is shown in Figure 16 (red line). As in the case of the 9.20 $M_{\odot}$ model, the first cooling phase is due to the activation of the ^{25}(Mg, Na) URCA pair. The cooling phase ends when the URCA shell shifts from the center outward in mass. Such an occurrence drives the formation of a convective core that progressively increases in mass. At variance with the 9.20 $M_{\odot}$ model, in this case, the ^{25}Mg ingested from the radiative zones above the convective core is high enough to induce a TIR before the threshold density for the activation of the ^{23}(Na, Ne) URCA pair is reached. During the TIR, the central ^{25}Mg mass fraction increases by ∼3 orders of magnitude, i.e., from $\log X_c \simeq -5.5$ to –2.5, while the central temperature increases from $\log[T_c\ (\mathrm{K})] \simeq 8.3$ to 8.75 (Figure 27). As for the 9.20 $M_{\odot}$ model, in this case the TIR is followed by a phase in which the central abundance of the leading isotope (in particular ^{23}Na for the 9.20 $M_{\odot}$ and ^{25}Mg for the 9.15 $M_{\odot}$ cases, respectively) decreases progressively, and the extra energy provided by the TIR is progressively reabsorbed. This stage also coincides with the onset of the thermal pulses. We stopped the calculation during this phase after the completion of 193 thermal pulses (see Table 4).

The evolution of the 9.10 $M_{\odot}$ star is similar to the one of the 9.15 $M_{\odot}$ star (Figure 28), and it is followed for 159 thermal pulses.

3.8. Final Fate of Stars with Initial Mass $7.50 \leqslant \mathrm{M/M_{\odot}} \leqslant 9.20$

During the thermal pulse phase, the CO core is continuously increased by the alternate advancing of the He- and H-burning shells. Such an occurrence induces an increase of the central density.

During the same stage, however, the star loses mass due to stellar wind, and this induces a progressive reduction of the H-rich envelope. If the CO core mass reaches the value ($M_{\mathrm{CO\text{-}ec}}$) corresponding to a central density close to the

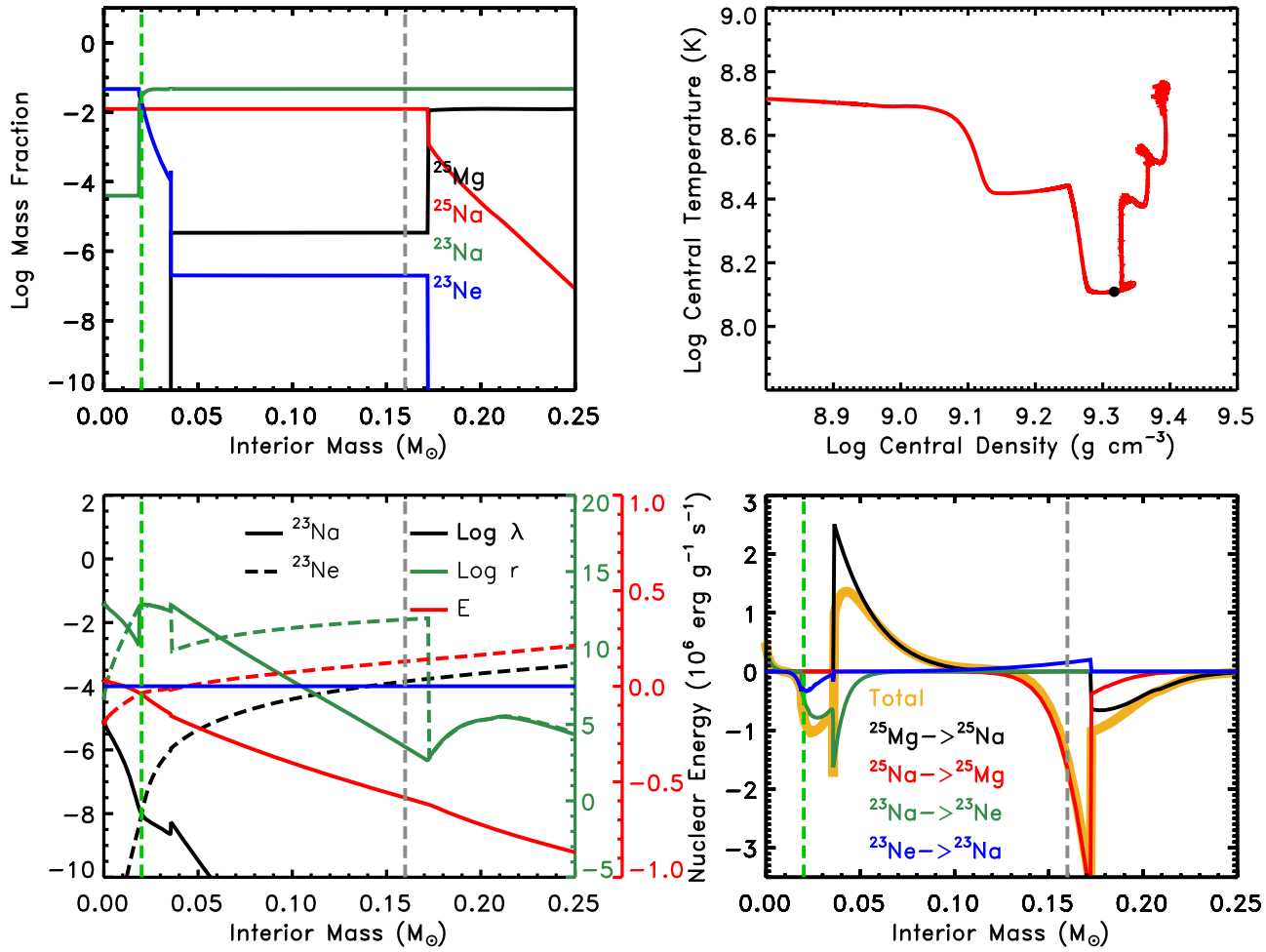

Figure 21. Same as Figure 20 but during a phase in which a convective core, driven by the ^{23}(Na, Ne) URCA pair, and a convective shell, induced by the ^{25}(Mg, Na) URCA pair, are formed. The gray and green vertical dashed lines mark the ^{25}(Mg, Na) and ^{23}(Na, Ne) URCA shells, respectively.

threshold value for the activation of the ^{24}Mg(e$^-$, ν)^{24}Na before the H-rich envelope is completely lost, the core contracts rapidly until the density approaches the threshold value for the activation of the ^{20}Ne(e$^-$, ν)^{20}Fe, and then the star can potentially explode as an ECSN (Miyaji et al. 1980; Nomoto 1987; Zha et al. 2019). If, on the contrary, the H-rich envelope is completely lost before the activation of the ECs on ^{24}Mg, then the final fate of the star will be as an ONeMg WD (Nomoto 1984). A self-consistent determination of the competition between the increase of the CO core mass and the reduction of the H-rich envelope due to the mass loss would require the calculation of several thousand thermal pulses, which, at present, is not feasible. Therefore, an estimate of the final fate of these stars must necessary rely on an "extrapolated" evolution.

Figure 29 shows the time evolution of the CO core mass (left panels) and the total mass (middle panels) for some selected models, i.e., 8.00, 8.50, 8.80, and 9.00 $M_\odot$, starting from the beginning of the thermal pulse phase. These two quantities show an almost linear behavior in the last part of the evolution that can be very well approximated by a linear regression (red lines in the left and middle panels of the figure). In the abovementioned panels, we also show the average values of the CO core mass growth rate and mass-loss rate obtained by such a linear regression. Under the assumption that the evolution following the last computed model will remain self-similar, we can easily extrapolate these quantities at late times (dashed lines in the right panels in the same figure). We are aware that when the envelope becomes sufficiently small, the strength of the pulses may change, and therefore the behavior of the CO core mass and the total mass may change accordingly. However, the importance of these effects, if they really exist, is difficult to predict a priori; therefore, as a working hypothesis, we assume a self-similar behavior of the relevant quantities up to the end of the evolution. The intersection of the two (extrapolated) lines, corresponding to the total mass and the CO core mass, is the maximum CO core mass ($M_{\rm CO-max}$, marked in the right panels of the figure with a black dot) that can be potentially formed before the envelope of the star is completely removed by the stellar mass loss. This quantity should be compared with $M_{\rm CO\text{-}ec}$, as defined above. An estimate of this last quantity can be obtained by solving the stellar structure equations for a completely degenerate star with a given mass M and a chemical composition typical of the zones interior to the CO core. In particular, we have taken the internal composition of the 9.00 $M_\odot$ star model as a representative one, being that slight variations of the chemical composition do not significantly affect the total mass–central density relation obtained in this way. By adopting the public code provided by F. X. Timmes,[9] we find that the mass

[9] Available at https://cococubed.com/code_pages/coldwd.shtml.

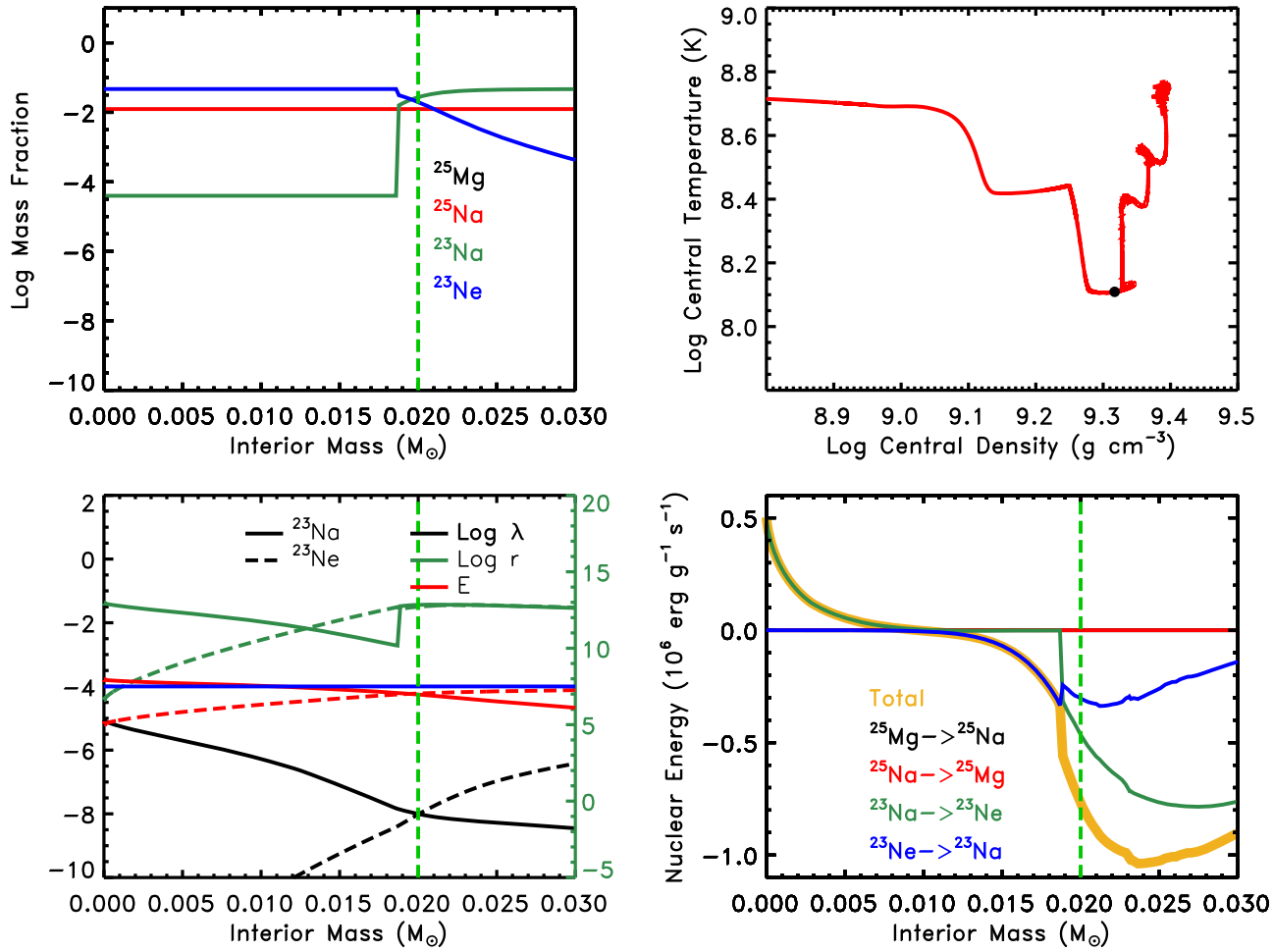

Figure 22. Same as Figure 21 but zoomed in on the inner 0.03 $M_{\odot}$.

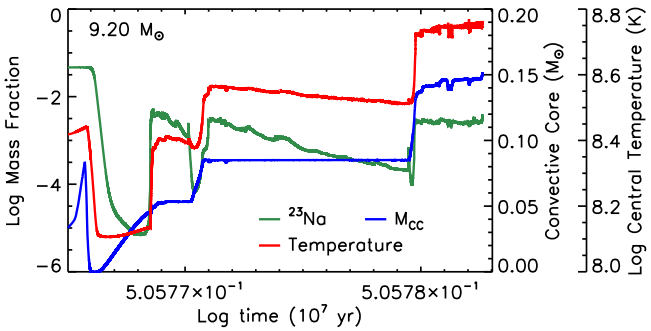

Figure 23. Selected quantities of the 9.20 $M_{\odot}$ model during the breathing pulses induced by the ^{23}(Na, Ne) URCA pair: the central ^{23}Na mass fraction (green line, left y-axis), the mass of the convective core (blue line, right y-axis), and the central temperature (red line, right y-axis).

corresponding to the threshold density ($\log[\rho_c\ (\mathrm{g\ cm^{-3}})] = 9.6$) for the activation of the ^{24}Mg(e$^-$, ν)^{24}Na is $M_{\mathrm{CO\text{-}ec}} = 1.415\,M_{\odot}$, while the Chandrasekhar mass is $M_{\mathrm{Ch}} \simeq 1.45\,M_{\odot}$. $M_{\mathrm{CO\text{-}ec}}$ is shown in the right panels of Figure 29 by a vertical blue dashed line. The right panels of the figure show that the minimum mass that can potentially explode as an ECSN is ∼8.5–8.8 $M_{\odot}$. Zha et al. (2019) obtained $M_{\mathrm{CO\text{-}ec}} = 1.36\,M_{\odot}$ in their evolutionary model, which pushes the minimum mass that can potentially explode as an ECSN to ∼8.3 $M_{\odot}$ in Figure 30. It is worth noting that for any given mass, the density obtained assuming that the structure is fully degenerate is the minimum one, the reason being that a progressive departure from degeneration allows for a progressively higher contraction and therefore larger central densities (for the same mass). This implies that the value of $M_{\mathrm{CO\text{-}ec}}$ marked by the blue dashed lines in the abovementioned figures constitutes an upper limit to this quantity.

Figure 30 shows the $M_{\mathrm{CO-max}}$ as a function of the initial mass compared to the $M_{\mathrm{CO\text{-}ec}}$. Also shown in the figure is the final ONeMg core mass as a function of the initial mass under the assumption that the ONeMg core does not increase during the thermal pulse phase because the accretion rate of the CO core is not high enough to induce further C burning (Nomoto & Iben 1985).

Taking into account all possible uncertainties, we conclude that stars in the range $7.50 \leqslant M/M_{\odot} \leqslant 8.00$ will lose their H-rich envelope before the threshold density for the EC on ^{24}Mg is achieved; therefore, they will produce an ONeMg WD. Stars in the range $8.50 \leqslant M/M_{\odot} \leqslant 9.20$, on the contrary, will reach such a critical density before the H envelope reduces enough to definitely quench the H-burning shell. Once the ^{24}Mg(e$^-$, ν)^{24}Na is activated, the final fate of these stars (explosion or collapse to a neutron star) depends on the details both of the explosion modeling and of the initial conditions (see Section 1) and cannot be predicted with certainty in this work. As a final comment, we point out that in stars with initial mass $9.10 \leqslant M/M_{\odot} \leqslant 9.20$, the central temperature increases substantially due to the TIR, and therefore the ignition of the

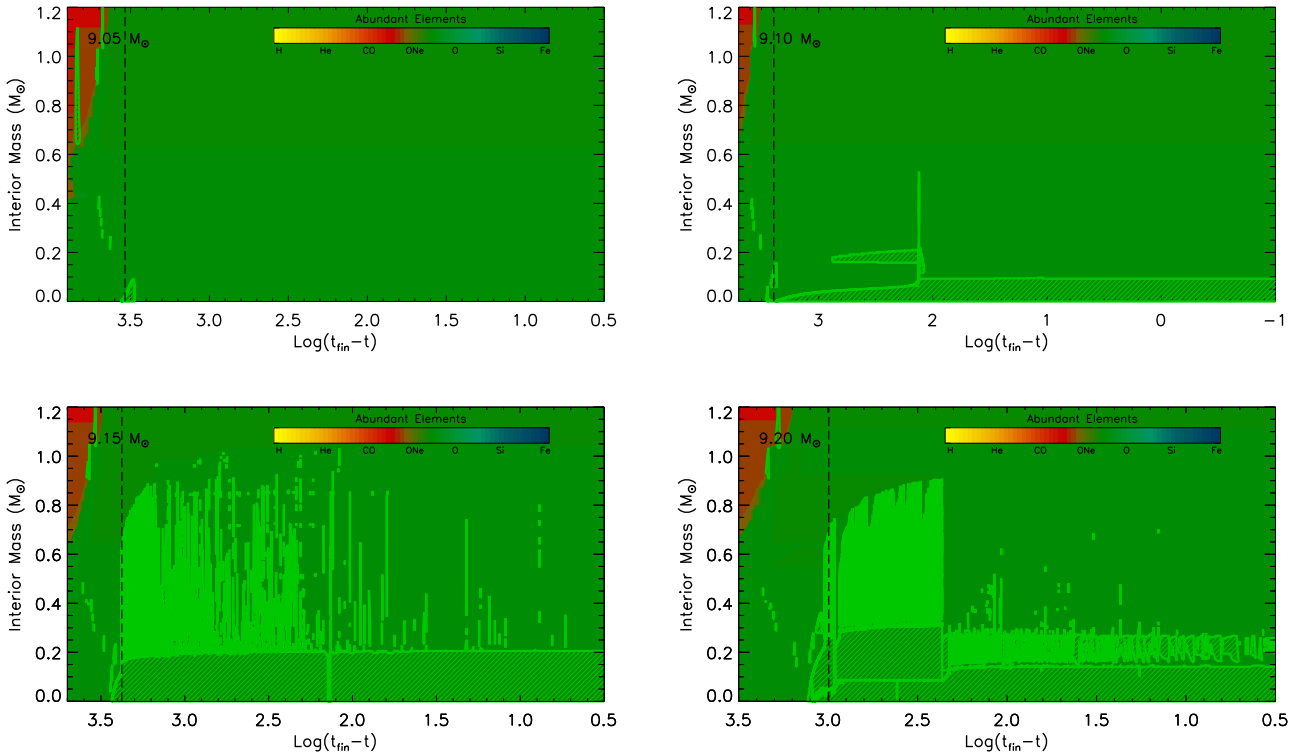

Figure 24. Convective (green shaded areas) and chemical (color codes reported in the color bar) internal history during the phase when the URCA processes are active. The x-axis reports the logarithm of the time until the end of the evolution ($t_{\rm fin} - t$) in units of years.

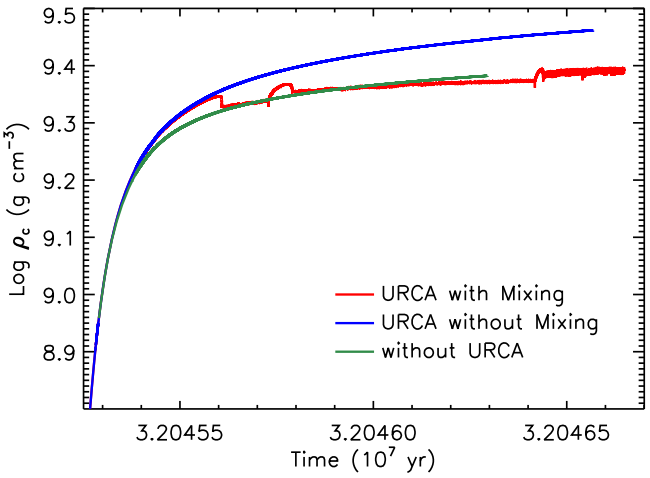

Figure 25. Evolution of the central density as a function of time for three models of the initial mass 9.20 $M_{\odot}$ prior the onset of the TIR (see text), computed with the following assumptions: URCA processes and convective mixing taken into account (reference model; red line), URCA processes taken into account and convective mixing artificially suppressed (blue line), and URCA processes neglected (green line).

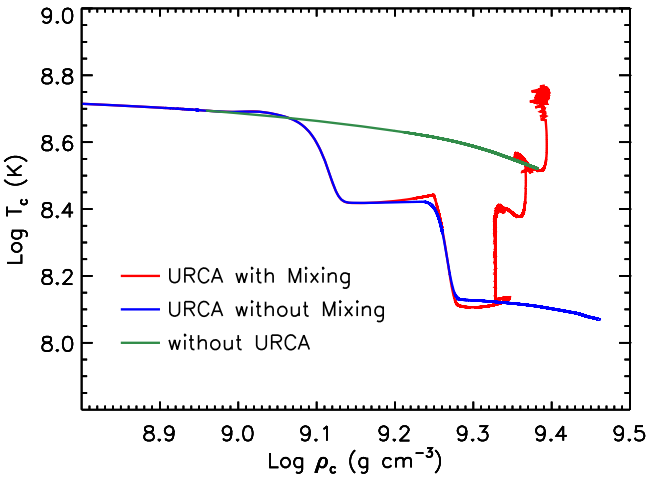

Figure 26. Evolution of the central temperature as a function of the central density for three models of initial mass 9.20 $M_{\odot}$ prior to the onset of the TIR (see text), computed with the following assumptions: URCA processes and convective mixing taken into account (reference model; red line), URCA processes taken into account and convective mixing artificially suppressed (blue line), and URCA processes neglected (green line).

^{20}Ne photodisintegration before the activation of the EC on ^{24}Mg cannot be excluded. In that case, it is difficult to predict, a priori, the final fate of these stars.

3.9. Evolution toward Core Collapse: Stars with $M \geqslant 9.22\,M_{\odot}$ *(*$M_{CO} \geqslant 1.08\,M_{\odot}$*)*

Stars with initial mass $M \geqslant 9.22\,M_{\odot}$ form an ONeMg core in which the maximum temperature reaches the threshold value for the Ne ignition. The thermal behavior of the ONeMg core depends on both the behavior of the C-burning shell and the convective history of the CO core, which, in turn, depend in general on the CO core mass at core He depletion. In the present set of models, we find that the minimum CO core mass at core He depletion for the activation of Ne burning is $M_{\rm CO} = 1.08\,M_{\odot}$, which corresponds to CO and ONeMg core masses at Ne ignition of $M_{\rm CO} = 1.363$ and $M_{\rm ONeMg} = 1.349\,M_{\odot}$, respectively (Figure 31 and Table 3). It is interesting to note that Ne ignition is activated before the ONeMg core (which coincides with the C-burning shell by definition) approaches the CO core (i.e., the He-burning shell), as happens in all of the models that do not ignite Ne and evolve through

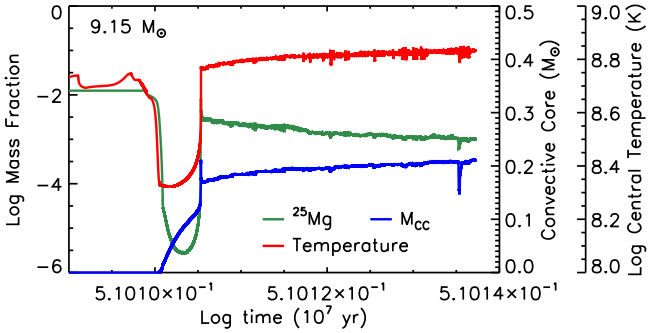

Figure 27. Same as Figure 23 but for the 9.15 $M_\odot$ model and during the TIR (see text) induced by the ^{25}(Mg, Na) URCA pair.

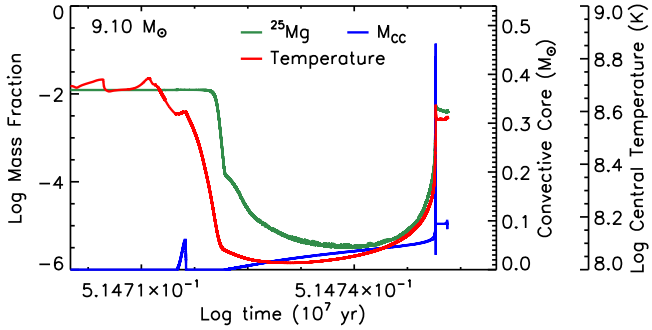

Figure 28. Same as Figure 27 but for the 9.10 $M_\odot$ model.

the SAGB phase. This is the reason why the ONeMg core mass versus the initial mass relation shows a small bending in the transition between SAGB stars and stars that do ignite Ne burning (Figure 31). As in the case of C ignition, the mass coordinate corresponding to the Ne ignition decreases progressively as the initial mass increases, ranging from 0.966 $M_\odot$ for 9.22 $M_\odot$ to 0 for 13 $M_\odot$, which is the lowest mass that ignites Ne at the center (Figure 12 and Table 3). Off-center Ne burning is ignited under conditions of sizable degeneracy ($\psi \sim 7$–5, in the mass range 9.22–12.00 $M_\odot$); therefore, the local nuclear energy release drives a progressive increase of both the temperature and the luminosity and, as a consequence, the formation of a convective zone. Such a convective zone reaches a maximum extension and then tends to recede in mass as the Ne is progressively depleted. In the lower-mass models (9.22–9.30 $M_\odot$), during this phase, the temperature approaches values as high as log$T$ (K) $\sim$ 9.3; therefore, O burning is also ignited before convection quenches. This drives the convective zone to increase again up to a maximum extension. After the O ignition, the Ne/O burning proceeds simultaneously in a convective shell that progressively moves toward the center as the fuel is locally exhausted, the temperature is increased, and the degeneracy is significantly removed (left panel of Figure 32). In the more massive models (9.50–12.0 $M_\odot$), on the contrary, the local temperature does not reach the threshold values for O ignition; therefore, the first convective zone quenches and disappears as the Ne is depleted locally. After this first convective episode, contraction resumes, and another convective zone forms. From this time onward, the evolution of the Ne/O burning front in these more massive models is similar to the one described above for the lower-mass stars (see right panel of Figure 32).

Figures 33 shows the main properties of a typical model during the propagation of the Ne/O burning front toward the center. The burning is occurring at the base of the convective shell, marked by the gray area, which is at a high temperature compared to the inner, much cooler radiative zones. Because of the efficient ECs, the main products of the Ne/O burning within the convective shell are ^{34}S, ^{28}Si, ^{30}Si, and ^{32}S. The efficiency of the ECs, however, decreases as the initial mass of the star increases; therefore, the chemical composition left by the Ne/O burning tends to be dominated by less neutron-rich isotopes as the initial mass of the star increases. Figure 34 shows the chemical composition of selected models once the Ne/O burning front has reached the center.

In the 13.0 $M_\odot$ model, Ne burning is ignited at the center and develops in a convective core. Once Ne is depleted in the center, the burning shifts outward in mass, in the region with a variable composition left by the receding convective core, and drives the formation of a convective shell at a mass coordinate of $\sim$0.18 $M_\odot$. During this phase, the temperature in the shell increases enough that O burning is ignited. Ne and O burning then proceed simultaneously in such a shell, which increases progressively in mass up to a maximum extension of 0.17–1.00 $M_\odot$. Once O is exhausted in the shell, the burning shifts inward and drives the formation of a convective core that reaches a maximum extension of $\sim$0.07 $M_\odot$ before disappearing at O depletion. Ne and O burning develop in the 15.0 $M_\odot$ model as in a typical MS.

It is interesting to note at this point that, at variance with off-center C burning, no hybrid core is formed as a result of the off-center Ne ignition. All of the stars that ignite off-center Ne burning form an O-depleted core; i.e., in all of these models, the ONe burning front reaches the center. This result is consistent with what has been found by Woosley & Heger (2015) and can be understood because we are using a similar approach to treat the CBF. On the contrary, Jones et al. (2013) found a case in which the ONe burning front does not propagate toward the center, leading the star to reach central densities high enough for the activation of the EC on ^{20}Ne and then to explode as an ECSN. This different behavior can be due to the fact that Jones et al. (2013) do not include in the code any specific treatment for the CBF; therefore, their models cannot be directly compared to ours.

In the 9.22 $M_\odot$ star, after the Ne/O burning front has reached the center, the most abundant nuclear species in the O-exhausted core are ^{34}S ($\sim$0.48), ^{38}Ar ($\sim$0.22), ^{28}Si ($\sim$0.16), and ^{30}Si ($\sim$0.13; left panel of Figure 34). O burning that shifts in a shell settles at a mass coordinate of $\sim$0.6 $M_\odot$, where O is still quite abundant. Shell O burning moves outward in mass, inducing the formation of three consecutive convective shells. During this phase, in the inner core, ^{38}Ar and ^{28}Si are converted into ^{34}S and ^{30}Si, which increase to $\sim$0.70 and $\sim$0.28 in mass fraction, respectively. When the O-burning shell has reached $\sim$1.30 $M_\odot$, nuclear burning is ignited at $\sim$0.95 $M_\odot$ at a temperature of $\sim 3 \times 10^9$ K (Figure 35 shows the physical and chemical structure of the star at this stage).

During the initial phase of this burning, the rearrangement of the matter is such that ^{34}S and ^{30}Si are depleted while ^{28}Si, ^{52}Cr, ^{54}Fe, and ^{56}Fe are produced in a convective shell that increases progressively in size. Once ^{34}S and ^{30}Si are exhausted in the shell, convection quenches and the nuclear burning front shifts inward in mass, where ^{34}S and ^{30}Si are still abundant, and induces the formation of a convective shell that, once again, reaches a maximum extension and then quenches. The burning front, then, propagates in this way progressively toward the center. A typical model during this phase in shown in

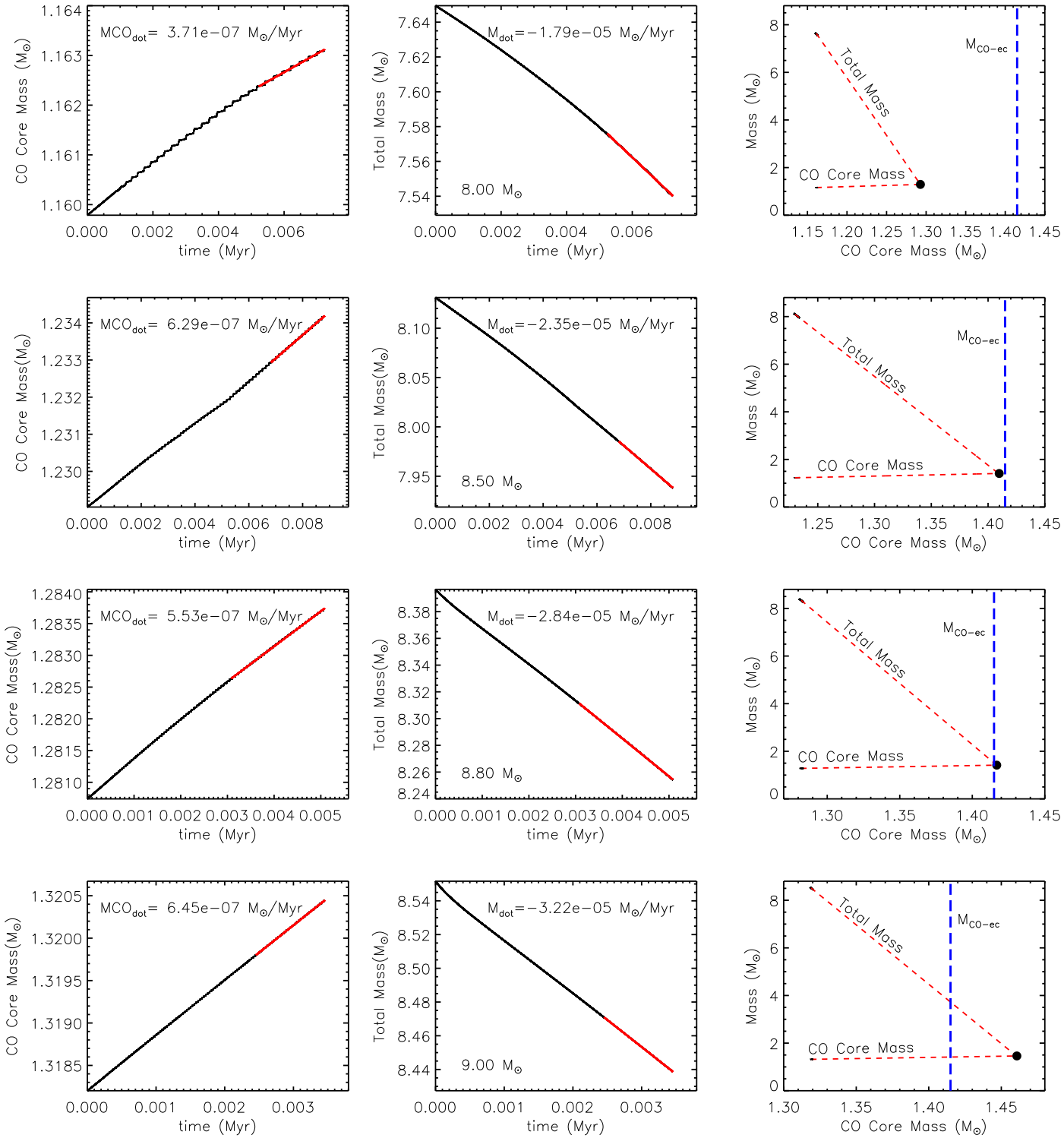

Figure 29. CO core mass (left panels) as a function of time, total mass (middle panels) as a function of time, and total mass as a function of CO core mass (right panels) for the 8, 8.50, 8.80, and 9.00 $M_{\odot}$ models (top to bottom). The time has been reset at the beginning of the thermal pulses. The solid red line in the left and middle panels refers to the linear regression of the black line over the last few thermal pulses, superimposed on the black line itself. The values reported in the plots (MCO_{dot} and M_{dot}) refer to the rate of growth of the CO core and the rate of mass loss obtained with the linear regression. The dashed lines in the right panels refer to the extrapolation at late times of the various quantities shown in the figure, obtained with the linear regression mentioned before. The vertical blue dashed line marks the CO core mass corresponding to the central density threshold for the activation of the EC on ^{24}Mg derived as discussed in the text (Zha et al. 2019).

Figure 36. As the ^{34}S–^{30}Si burning front moves inward in mass, the interplay between local burning and convective mixing is such that ^{52}Cr tends to be the dominant nuclear species, followed by ^{30}Si and ^{34}S, not completely depleted, and finally by ^{56}Fe. The physical and chemical structure of the star once the burning front has reached the center is shown in Figure 37. The residual ^{28}Si (∼0.02 in mass fraction) is then eventually burned in a convective core that increases in size up to ∼0.9 $M_{\odot}$ and leaves a chemical composition dominated by ^{52}Cr (∼0.60) and ^{56}Fe (∼0.28).

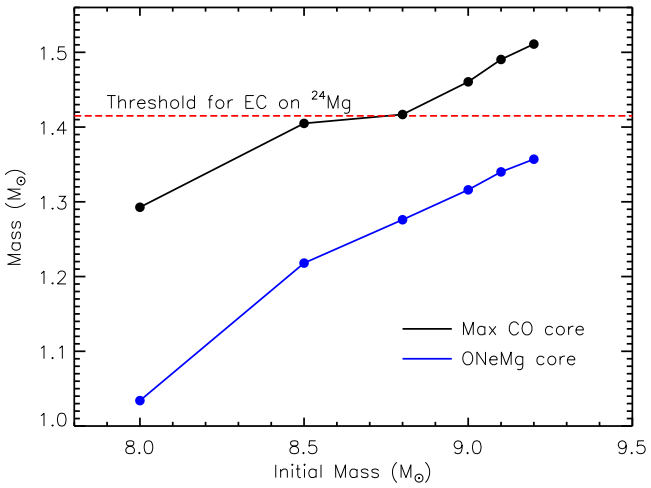

Figure 30. Final CO and ONeMg core masses obtained with the "extrapolated evolution" based on a linear regression (see text). Also shown is the CO core mass corresponding to the threshold central density for the activation of the EC on ^{24}Mg.

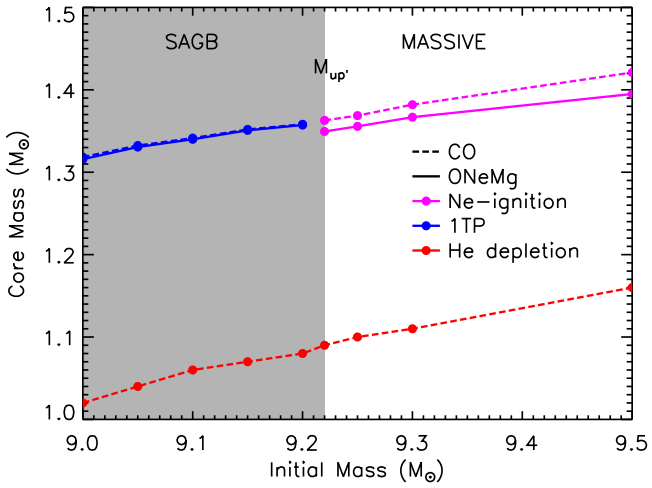

Figure 31. CO (dashed line) and ONeMg (solid line) core mass as a function of the initial mass at various evolutionary stages: core He depletion (red line and dots), first thermal pulse (blue line and dots), and Ne ignition (magenta line and dots).

During the following evolution, the core contracts and heats up, and the matter is converted to iron peak (Fe) isotopes. The composition of the Fe core is dominated by the most abundant isotopes of matter at the nuclear statistical equilibrium corresponding to progressively higher values of the temperature and density and progressively lower values of the electron fraction due to the efficient ECs. The Fe core mass at the presupernova stage is $M_{\rm Fe} = 1.257\,M_\odot$, and its composition is dominated by ^{50}Ti, ^{54}Cr, and ^{58}Fe (Figure 38). All of the other relevant physical quantities of the model at the presupernova stage are reported in Table 3.

The evolution of the stars in the range 9.25–12.0 $M_\odot$ after the Ne/O burning front has reached the center and up to the presupernova stage is similar to that of 9.22 $M_\odot$. The only difference is the mass coordinate corresponding to the Si–S ignition. In particular, in the models with mass in the range 9.25–9.50 $M_\odot$, the Si–S is ignited at a mass coordinate that progressively decreases as the mass increases; i.e., it is ∼0.52, ∼0.07, and ∼0.005 $M_\odot$ for 9.25, 9.30, and 9.50 $M_\odot$, respectively (see Table 3).

In the models with mass in the range 9.80–12.0 $M_\odot$, the ^{28}Si is not completely exhausted in the inner core during the shell O burning, as it happens in the lower-mass models, and it shows a gradient (see Figure 39). The sizable abundance of ^{28}Si and its profile induces an off-center nuclear ignition at a mass coordinate that decreases as the initial mass increases, ranging from ∼0.387 $M_\odot$ for 9.80 $M_\odot$ to 0 for 13.0 $M_\odot$, which is the lowest-mass model that ignites Si burning centrally and behaves during this phase as a typical MS. The 10.0 $M_\odot$ model is an outlier in this scheme because for some reason, difficult to understand, a sizable abundance of ^{28}Si ∼ 0.19 (in mass fraction) is left in the center (in the inner ∼0.020 $M_\odot$) at the end of the shell O-burning phase; therefore, in this model, the Si ignition point is more internal than in either the 9.80 or 11.0 $M_\odot$ model (Table 3).

Table 3 reports all of the main physical properties of all of these models at the presupernova stage.

4. Summary and Conclusions

In this paper, we computed the evolution of stars with initial mass in the range 7.00–15.00 $M_\odot$ from the pre-main-sequence phase up to the presupernova stage or an advanced stage of the TP phase, depending on the initial mass. The main goal of these calculations is to study in detail the evolutionary behavior of stars across the transition from AGB and SABG stars to ECSN and CCSN progenitors.

A summary of our results is shown in Figure 40 and discussed below.

All the stars in the mass range studied here evolve through the core H- and He-burning stages.

Stars with initial mass $M < 7.50\,M_\odot$ develop a degenerate CO core in which the temperature remains below the threshold value for the ignition of the C-burning reactions. These stars then evolve through the TP-AGB phase and eventually end their evolution by forming a CO WD surrounded by material ejected during the previous evolutionary phases, i.e., a planetary nebula.

In stars with initial mass $M \geqslant 7.50\,M_\odot$, on the contrary, the temperature in the CO core becomes high enough to allow the ignition of the C-burning reactions. In particular, stars with initial mass in the range 7.50–9.50 $M_\odot$ ignite C off-center, with the C ignition point decreasing from 0.588 $M_\odot$ for 7.50 $M_\odot$ to 0.022 $M_\odot$ for 9.50 $M_\odot$. Stars with initial mass $M > 9.50\,M_\odot$ ignite C centrally. This feature is mainly due to the fact that the degree of degeneracy in the CO core decreases progressively as the initial mass increases. In all of the stars, the result of the C burning is the production of an ONeMg core, with the exception of the 7.50 $M_\odot$ star, in which the C-burning front quenches before reaching the center, and therefore a sizable amount of ^{12}C is left unburned in the inner ∼0.3 $M_\odot$. In this case, a hybrid CO core is formed, i.e., a CO core in which the central part is enriched by a mixture of O and Ne, resulting from the quenching of the off-center C burning.

After core He depletion, in stars with initial mass $M < 11.00\,M_\odot$, the convective envelope penetrates into the He layer, and the second dredge-up takes place. The evolutionary stage at which this phenomenon begins and goes to completion (i.e., when the convective envelope reaches the maximum depth) depends on the initial mass. In particular, it begins (1) after core He depletion for the 7.00 $M_\odot$ star, (2) before C ignition for the 7.50–8.00 $M_\odot$ stars, and (3) after C ignition for the 8.50–10.00 $M_\odot$ stars. The convective envelope

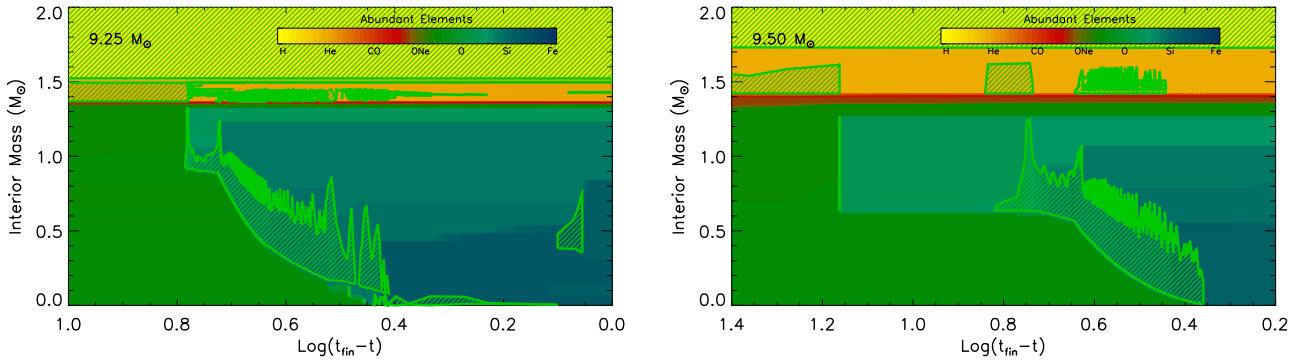

Figure 32. Convective (green shaded areas) and chemical (color codes reported in the color bar) internal history during off-center Ne burning for the 9.25 $M_\odot$ (left panel) and 9.50 $M_\odot$ (right panel) models. The x-axis reports the logarithm of the time until the end of the evolution ($t_{\rm fin} - t$) in units of years.

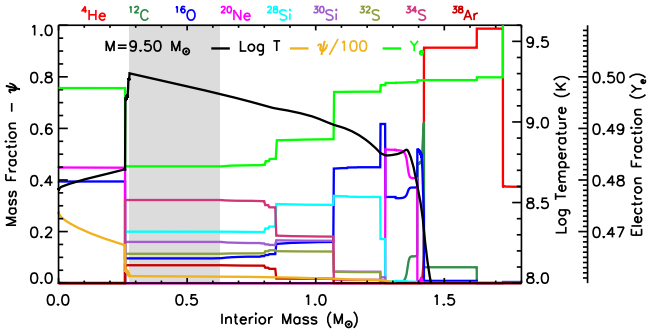

Figure 33. Selected chemical and physical properties (see the legend) of the 9.50 $M_\odot$ model during the off-center neon burning.

reaches its maximum depth during the second dredge-up (1) before the beginning of the TP phase for the 7.00 $M_\odot$ star and (2) after the C-burning phase for the 7.50–10.00 $M_\odot$ stars.

In stars with initial mass in the range 7.50–9.20 $M_\odot$, the maximum temperature in the ONeMg core (the hybrid CO core for 7.50 $M_\odot$) does not reach the threshold value for the ignition of Ne burning. Therefore, these stars evolve through the TP-SAGB phase. As the initial mass increases, the maximum luminosity of the He-burning shell reached during each pulse decreases, while the frequency of the thermal pulses increases. This is due to the increasing size of the ONeMg core with the initial mass. This also implies that the third dredge-up, i.e., the penetration of the convective envelope into the He core, decreases progressively as the initial mass increases, disappearing for stars with $M \geqslant 9.00\,M_\odot$. In stars with initial mass in the range 9.05–9.20 $M_\odot$, the central density becomes high enough that the URCA pair ^{25}(Mg–Na) is activated. This induces a cooling of the center of the star while the core is still contracting followed by a phase of contraction at constant temperature. In the 9.20 $M_\odot$ star, the density increases enough to reach the threshold for the activation of the URCA pair ^{23}(Na–Ne). Also in this case, the center initially cools down and then evolves at constant temperature. During these phases, a convective core forms and progressively increases in mass, causing, in stars with mass 9.10–9.20 $M_\odot$, a phenomenon similar to the breathing pulses in core He burning. This phenomenon happens after the activation of the ^{25}(Mg–Na) URCA pair, in stars with initial mass 9.10–9.15 $M_\odot$, and after the activation of the ^{23}(Na–Ne) URCA pair in the 9.20 $M_\odot$ model and induces a substantial increase of the central temperature (TIR). The final fate of all of these stars that do not ignite Ne burning depends on the competition between the increase of the CO core, which may lead to the potential explosion of the star once the central density reaches the threshold value for the ignition of the EC on ^{24}Mg, and the reduction of the envelope due to the mass loss. The detailed calculation of such a competition would require the calculation of several thousands of thermal pulses (together with the URCA pairs in the more massive ones), which is not feasible with the network adopted in this work and the computers presently available. For this reason, the final fate of these stars has been estimated by means of "extrapolated" evolutions. According to these extrapolations, and taking into account all of the possible uncertainties, we predict that in stars with initial mass in the range 7.50–8.00 $M_\odot$, the mass loss is efficient enough to reduce the total mass before the CO mass reaches the critical value for the activation of the EC on ^{24}Mg. These stars, therefore, will end their lives producing ONeMg WDs (a hybrid CO WD in the 7.50 $M_\odot$ star case). Stars with initial mass in the range 8.50–9.20 $M_\odot$ develop CO cores massive enough to reach the activation of the EC on ^{24}Mg before the envelope is completely removed by the mass loss and therefore can explode as ECSNe or collapse to a neutron star; the actual outcome depends on the details of the explosion modeling and the initial conditions and cannot be predicted with certainty in this work. Let us eventually remark that in stars with initial mass 9.10–9.20 $M_\odot$, the increase of the central temperature due to the TIR up to the threshold value for the ignition of the ^{20}Ne photodisintegration, before the activation of the EC on ^{24}Mg, cannot be excluded. In such a case, the prediction of the final fate of these stars is difficult to predict a priori.

In stars in the mass range 9.22–15.00 $M_\odot$, the maximum temperature in the ONeMg core reaches the threshold value for the ignition of Ne burning. In stars with initial mass in the range 9.22–12.00 $M_\odot$, Ne burning is ignited off-center, with the mass coordinate of the ignition point decreasing progressively with increasing mass. The off-center Ne ignition induces the temperature to increase above the threshold value for the ignition of O burning; therefore, in these stars, Ne and O burning occurs simultaneously. The Ne/O burning front then shifts progressively toward the center until an O-exhausted core is formed. Note that, at variance with the off-center C ignition, no hybrid core is formed as a result of the off-center Ne/O burning. In stars with mass $M \geqslant 13.00\,M_\odot$, the Ne burning is ignited centrally. While in the 13.00 $M_\odot$ star, Ne and O burning occur simultaneously, in the 15.00 $M_\odot$ star, they develop in two different stages, as happens in the classical MSs. Also in these stars, the final result of Ne and O burning is the formation of an O-exhausted core.

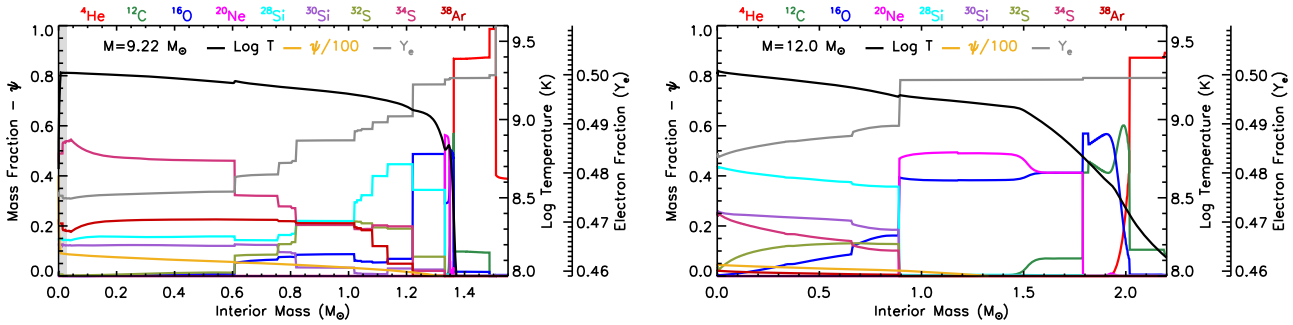

Figure 34. Selected chemical and physical properties (see the legend) of the 9.22 $M_{\odot}$ (left panel) and 12.0 $M_{\odot}$ models when the ONe burning front has reached the center.

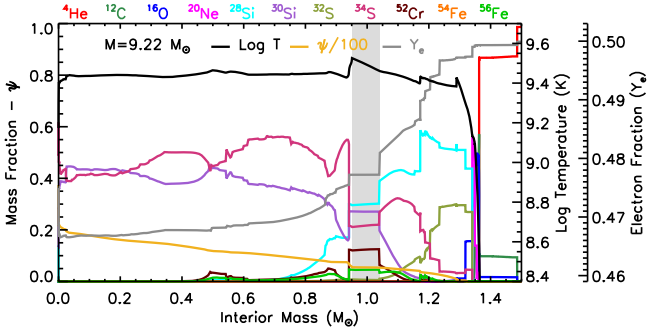

Figure 35. Selected chemical and physical properties (see the legend) of the 9.22 $M_{\odot}$ star at off-center Si–S ignition.

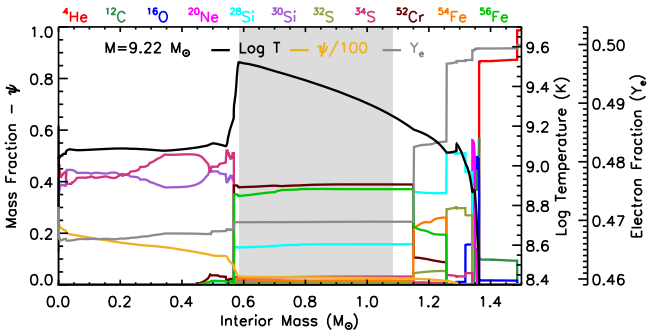

Figure 36. Selected chemical and physical properties (see the legend) of the 9.22 $M_{\odot}$ star during the off-center Si–S burning.

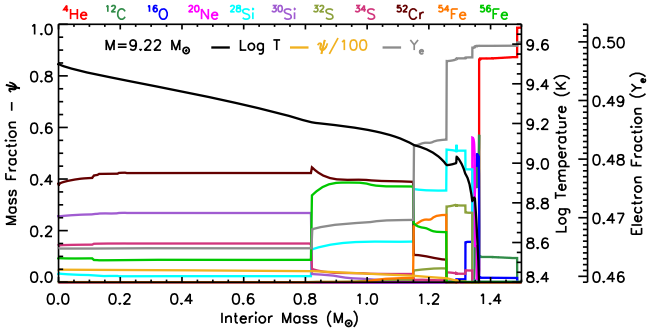

Figure 37. Selected chemical and physical properties (see the legend) of the 9.22 $M_{\odot}$ star when the Si–S burning front has reached the center.

The evolution after either center and off-center Ne/O burning is characterized by the O-shell burning that shifts progressively outward in mass and leads to the Si–S ignition. This burning starts off-center in stars with initial mass in the

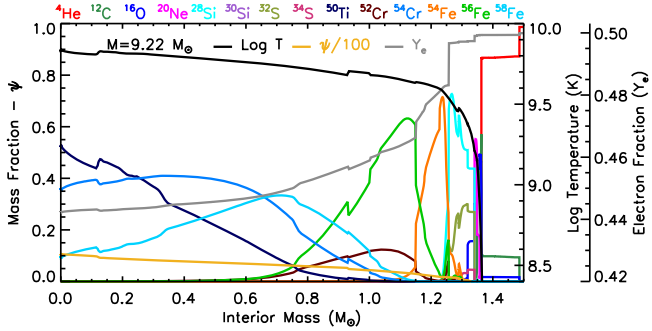

Figure 38. Selected chemical and physical properties (see the legend) of the 9.22 $M_{\odot}$ star at the presupernova stage.

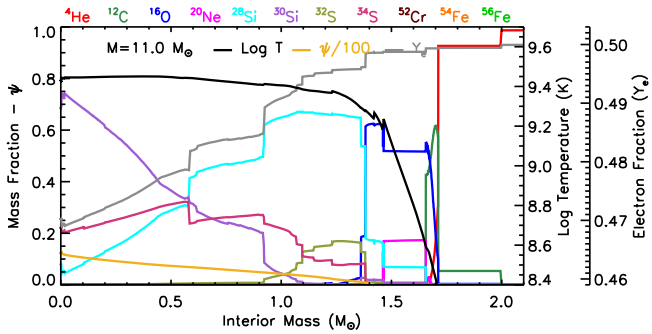

Figure 39. Selected chemical and physical properties (see the legend) of the 11.0 $M_{\odot}$ model during the shell O-burning phase.

range 9.22–12.00 $M_{\odot}$, and the main fuel is ^{34}S and ^{30}Si in the lower-mass models (9.22–9.50 $M_{\odot}$) and ^{28}Si in the more massive ones. This is due to the fact the lower-mass models evolve at lower entropy and therefore in these stars, the ECs are more efficient in reducing the electron fraction. As in other previous off-center burning, in this case the Si–S burning front propagates toward the center, followed by a shell Si–S burning phase, until an Fe core is formed. Also in this case, the Si–S burning front does not quench before reaching the center; therefore, no hybrid Si–S core is formed. Si burning is ignited centrally in stars with initial mass $M \geqslant 13.00\,M_{\odot}$ and is followed by a shell Si-burning phase like in the classical MSs until an Fe core is formed. The final fate of all of the stars in the mass range 9.22–15.00 $M_{\odot}$ is therefore explosion as CCSNe. As a final comment, let us note that the luminosity of the lower-mass star that explodes as a CCSN (see Figure 2) is compatible with the estimate of the minimum luminosity for the progenitors of SNIIP derived from the analysis of the high-

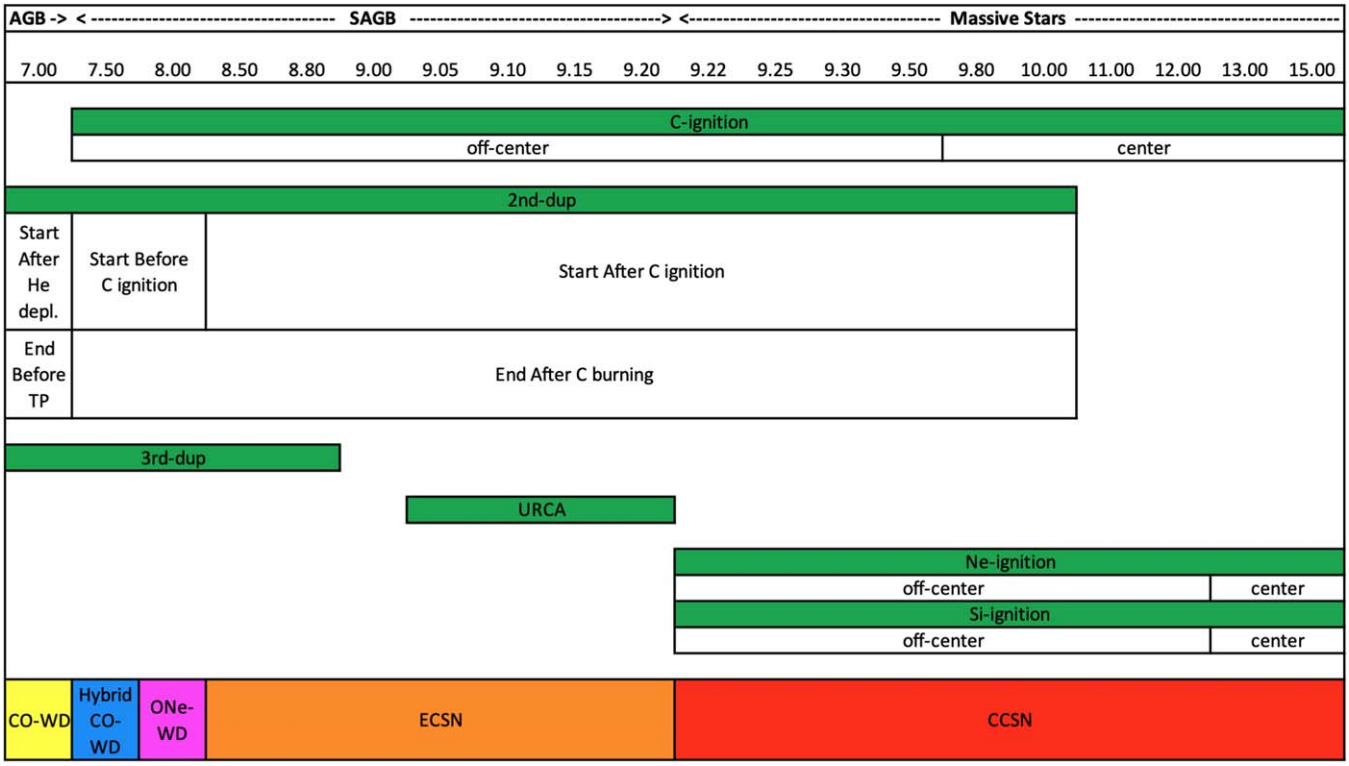

Figure 40. Schematic view of some of the evolutionary properties and expected final fate.

resolution images obtained by space- and ground-based telescopes (Smartt 2015).

Acknowledgments

This work has been mainly supported by the Theory Grant "Evolution, nucleosynthesis and final fate of stars in the transition between AGB and Massive Stars" (PI: M. Limongi) of the INAF Fundamental Astrophysics Funding Program 2022–2023. This work has also been partially supported by the World Premier International Research Center Initiative (WPI), MEXT, Japan. K.N. has been supported by Japan Society for the Promotion of Science (JSPS) KAKENHI grants JP20K04024, JP21H04499, and JP23K03452. M.L. warmly thanks Toshio Suzuki for providing clarifications on the correct use of the weak rates for the electron capture and beta decays of the URCA processes.

ORCID iDs

Marco Limongi https://orcid.org/0000-0003-0636-7834
Lorenzo Roberti https://orcid.org/0000-0003-0390-8770
Alessandro Chieffi https://orcid.org/0000-0002-3589-3203
Ken'ichi Nomoto https://orcid.org/0000-0001-9553-0685

References

Asplund, M., Grevesse, N., Sauval, A. J., & Scott, P. 2009, ARA&A, 47, 481
Bertelli, G., Bressan, A., Chiosi, C., et al. 1986, A&AS, 66, 191
Blöcker, T. 1995, A&A, 297, 727
Bressan, A. G., Chiosi, C., & Bertelli, G. 1981, A&A, 102, 25
Brinkman, H. E., Doherty, C., Pignatari, M., Pols, O., & Lugaro, M. 2023, ApJ, 951, 110
Caputo, F., Castellani, V., Chieffi, A., et al. 1989, ApJ, 340, 241
Castellani, V., Chieffi, A., Tornambè, A., et al. 1985, ApJ, 296, 204
Chieffi, A., & Limongi, M. 2013, ApJ, 764, 21
Chieffi, A., & Limongi, M. 2020, ApJ, 890, 43
Chieffi, A., & Straniero, O. 1989, ApJS, 71, 47
Doherty, C. L., Gil-Pons, P., Lau, H. H. B., et al. 2014, MNRAS, 437, 195
Doherty, C. L., Gil-Pons, P., Siess, L., et al. 2015, MNRAS, 446, 2599
Doherty, C. L., Gil-Pons, P., Siess, L., et al. 2017, PASA, 34, e056
Duchêne, G., & Kraus, A. 2013, ARA&A, 51, 269
Fischer, T., Whitehouse, S. C., Mezzacappa, A., et al. 2010, A&A, 517, A80
Gil-Pons, P., Doherty, C. L., Lau, H., et al. 2013, A&A, 557, A106
Hiramatsu, D., Howell, D. A., Van Dyk, S. D., et al. 2021, NatAs, 5, 903
Isern, J., Canal, R., & Labay, J. 1991, ApJL, 372, L83
Jones, S., Hirschi, R., Nomoto, K., et al. 2013, ApJ, 772, 150
Jones, S., Hirschi, R., & Nomoto, K. 2014, ApJ, 797, 83
Jones, S., Ritter, C., Herwig, F., et al. 2016, MNRAS, 455, 3848
Jones, S., Röpke, F. K., Pakmor, R., et al. 2016, A&A, 593, A72
Karakas, A. I., García-Hernández, D. A., & Lugaro, M. 2012, ApJ, 751, 8
Kitaura, F. S., Janka, H.-T., & Hillebrandt, W. 2006, A&A, 450, 345
Lau, H. H. B., Gil-Pons, P., Doherty, C., et al. 2012, A&A, 542, A1
Limongi, M., & Chieffi, A. 2006, ApJ, 647, 483
Limongi, M., & Chieffi, A. 2018, ApJS, 237, 13
Miyaji, S., & Nomoto, K. 1987, ApJ, 318, 307
Miyaji, S., Nomoto, K., Yokoi, K., et al. 1980, PASJ, 32, 303
Ning, H., Qian, Y.-Z., & Meyer, B. S. 2007, ApJL, 667, L159
Nomoto, K. 1984, ApJ, 277, 791
Nomoto, K. 1987, ApJ, 322, 206
Nomoto, K. 2014, in IAU Symp. 296, Supernova Environmental Impacts, ed. A. Ray & A. McCray (Cambridge: Cambridge Univ. Press), 27
Nomoto, K., & Hashimoto, M. 1988, PhR, 163, 13
Nomoto, K., & Iben, I. 1985, ApJ, 297, 531
Nomoto, K., & Kondo, Y. 1991, ApJL, 367, L19
Nomoto, K., & Leung, S.-C. 2017, in Handbook of Supernovae, ed. A. Alsabti & P. Murdin (Cham: Springer), 483
Nomoto, K., Sparks, W. M., Fesen, R. A., et al. 1982, Natur, 299, 803
Nomoto, K., & Sugimoto, D. 1972, PThPh, 48, 46
Radice, D., Burrows, A., Vartanyan, D., et al. 2017, ApJ, 850, 43
Ritossa, C., García-Berro, E., & Iben, I. 1999, ApJ, 515, 381
Roberti, L., Limongi, M., & Chieffi, A. 2024, ApJS, 270, 28
Siess, L. 2007, A&A, 476, 893
Siess, L. 2010, A&A, 512, A10
Smartt, S. J. 2009, ARA&A, 47, 63
Smartt, S. J. 2015, PASA, 32, e016
Sugimoto, D., & Nomoto, K. 1975, PASJ, 27, 197

Sugimoto, D., & Nomoto, K. 1980, SSRv, 25, 155
Suzuki, T., Toki, H., & Nomoto, K. 2016, ApJ, 817, 163
Takahashi, K., Sumiyoshi, K., Yamada, S., et al. 2019, ApJ, 871, 153
Takahashi, K., Yoshida, T., & Umeda, H. 2013, ApJ, 771, 28
Temaj, D., Schneider, F. R. N., Laplace, E., Wei, D., & Podsiadlowski, P. 2013, arXiv:2311.05701
Toki, H., Suzuki, T., Nomoto, K., et al. 2013, PhRvC, 88, 015806
Ventura, P., Carini, R., & D'Antona, F. 2011, MNRAS, 415, 3865
Ventura, P., Di Criscienzo, M., Carini, R., et al. 2013, MNRAS, 431, 3642
Woosley, S. E., & Heger, A. 2015, ApJ, 810, 34
Zha, S., Leung, S.-C., Suzuki, T., et al. 2019, ApJ, 886, 22
Zha, S., O'Connor, E. P., Couch, S. M., et al. 2022, MNRAS, 513, 1317